Diffusion and Solubility of Zinc in Dislocation-Free and Plastically Deformed Silicon Crystals[*]

D. Grünebaum[1], Th. Czekalla[1,], N. A. Stolwijk[1], H. Mehrer[1], I. Yonenaga[2], and K. Sumino[2]**

[1] Institut für Metallforschung, Westfälische-Wilhelms-Universität Münster, Wilhelm-Klemm-Strasse 10, W-4400 Münster, Fed. Rep. Germany
[2] Institute for Materials Research, Tohoku University, Katahira 2-1-1, Sendai 980, Japan

Abstract. Floating-zone Si crystals enclosed in quartz ampoules were exposed to Zn vapour released by an elemental diffusion source. Penetration profiles of Zn in Si were recorded using the spreading-resistance technique or neutron activation analysis. Both the erfc-type distributions observed in plastically deformed specimens and the non-erfc profiles determined on dislocation-free wafers are consistently interpreted within the framework of the kick-out model. As an implication, Si self-interstitials generated in excess by interstitial-to-substitutional transitions of in-diffusing Zn atoms annihilate not only at the surface but also at dislocations. On the other hand, dislocation-induced segregation of Zn appears to be rather minor, as revealed by transition electron microscopy. Combining the Zn incorporation rate in dislocation-free Si with solubility data from saturated specimens yields the self-interstitial contribution to the Si self-diffusion coefficient.

PACS: 61.70 Wp, 61.70 Yq, 64.75.+g, 66.30 Jt, 66.30 Lw

Considering foreign-atom diffusion in silicon we expect the behaviour of zinc to be particularly interesting. The $3d$ transition metals on the left side of Zn in the periodic table (V, ..., Cu) are known to dissolve and to migrate interstitially in the Si crystal [1–3]. By contrast, elements adjacent to Zn on the right hand side of the third row (Ga, Ge, As) have electronic and transport properties characteristic of substitutional incorporation [4]. This makes it likely that both a substitutional species (Zn_s) and an interstitial one (Zn_i) could be relevant for diffusion of Zn in Si. Indeed, in recent work preceding this study Perret et al. [5] found that at 1262 K Zn mainly diffuses by the kick-out mechanism [6], i.e.

$$Zn_i \rightleftharpoons Zn_s + I, \qquad (1)$$

where I denotes the Si self-interstitial.

Kick-out diffusion implies that accomodation of the more abundant foreign-atom configuration, i.e., the double acceptor Zn_s, requires three distinct steps: (i) long-range displacement in the form of Zn_i through the interstice, (ii) change-over to a substitutional site by pushing a Si atom aside, and (iii) transport of the so-created excess self-interstitial towards the surface, dislocations or other inner sinks, where it annihilates. For this reason kick-out diffusion has been found to be sensitive to the dislocation density of the Si crystals [7].

An alternative possibility for interstitital-substitutional exchange is given by the dissociative mechanism proposed in [8]:

$$Zn_i + V \rightleftharpoons Zn_s. \qquad (2)$$

Here the lattice vacancy (V) appears as the intrinsic point defect responsible for site exchange.

It is the aim of the present work to investigate the diffusion and solubility of Zn in Si over a wide temperature range. Both dislocation-free samples and plastically deformed crystals with high dislocation densities are used. Concentration-depth profiling is achieved by the (electrical) spreading-resistance technique (SRT) as well as by neutron activation analysis (NAA). Microstructural information emerges from transmission electron microscopy (TEM).

---

[*] Dedicated to H. J. Queisser on the occasion of his 60th birthday
[**] Now at: Krupp Atlas Elektronik GmbH, W-2800 Bremen 44

The experimental findings support the predominant role of the kick-out mechanism. Within this diffusion model we are able fo extract data from the penetration profiles which characterize the transport properties of interstitial Zn and Si atoms. The results are compared to those of Au, which is also known to diffuse by the kick-out process in Si.

1. Experimental

1.1 Materials Characterization

Dislocation-free specimens were cut from floating-zone (FZ) silicon with carbon contents below $5 \times 10^{20} \, \mathrm{m}^{-3}$ and oxygen concentrations less than $1 \times 10^{22} \, \mathrm{m}^{-3}$. (i) Boron-doped material had a resistivity of about $17 \, \Omega\mathrm{m}$ and was oriented in the $\langle 100 \rangle$ direction. (ii) Phosphorus-doped wafers were characterized by a $3 \, \Omega\mathrm{m}$ resistivity and a $\langle 111 \rangle$ orientation.

Plastically deformed crystals were made by mechanical compression of 20 mm long, $\langle 123 \rangle$ oriented bars of FZ Si [9]. This treatment was carried out at 1073 K under vacuum or inert gas atmosphere within time periods of 4–5 h. (iii) $8 \times 8 \, \mathrm{mm}^2$ wide cuboids of phosphorus-doped Si with resistivities in the range 18–27 $\Omega\mathrm{m}$ were deformed by roughly 10% in Sendai. (iv) Rods, consisting of 41 $\Omega\mathrm{m}$ boron-doped material with a $4 \times 4 \, \mathrm{mm}^2$ cross-section were compressed by about 5% at the Universität Köln. So-obtained dislocation densities are estimated to be at least $1 \times 10^{12} \, \mathrm{m}^{-2}$. In both cases specimens for diffusion experiments were cut perpendicularly to the long $\langle 123 \rangle$ axis.

1.2 Preparation and Annealing

Specimens with thicknesses between 0.3 mm and 5 mm were lapped in subsequents steps starting with 15 μm grade and ending with 1 μm grade alumina powder. In many cases additional polishing was carried out. However, no pronounced differences between lapped and polished specimens were observed, which contradicts an earlier suggestion [5] that the diffusion behaviour may be affected by surface conditions.

After etching and cleaning, the specimens were enclosed in quartz ampoules which also contained argon and chips of 6N pure zinc as the diffusion source. For ampoule volumes between $5 \times 10^{-6} \, \mathrm{m}^{-3}$ and $15 \times 10^{-6} \, \mathrm{m}^{-3}$ and specimen masses of typically 100 mg the Zn weight was in the range 15–60 mg. Such amounts were usually sufficient to build up a Zn partial pressure in (quasi-) equilibrium with the pure Zn source or the SiZn liquid which will be formed on the specimen surface according to the phase diagram. On the other hand, in most cases the amount of Zn proved to be small enough to avoid melting away of substantial specimen portions. Moreover, in some of the NAA experiments the addition of Si powder encapsulated by an open inner ampule led to a reduction of the surface damage caused by ZnSi alloy formation. Above about 1520 K the decreasing strength of quartz did not permit the high Zn pressure that would correspond to equilibrium with the condensed Zn source (about 12 atm at 1500 K) to be attained. Hence the boundary or saturation concentrations measured on specimens diffused at the highest temperatures do not correspond to the maximum solubilities determined at lower temperatures.

Diffusion anneals were conducted in resistance furnaces with temperature stabilities better than 1 K. Absolute temperature was monitored as close as possible to the specimens by means of calibrated thermocouples. Cooling down within roughly 10 s was achieved by plunging the ampoules into water at room temperature. When necessary, a correction for heating-up delay was applied.

In many cases the (encapsulated) specimens were subjected to a second anneal of 1/4 h at 889 K. As evidenced by DLTS work [10–12] this treatment serves to transform unidentified Zn(X) complexes into the isolated substitional Zn atoms without noticeably changing the total Zn content by out-diffusion. Probably, 889 K-annealing allows unwanted transition metal impurities to be released from binding to Zn$_s$ and subsequently to diffuse towards the surface. It should be noted that ZnCr and ZnCu pairs have been detected by EPR in our diffused specimens [13].

1.3 Spreading-Resistance Technique

Depth profiling was done with the aid of an automatically stepping two-point probe (Solid State Measurements, ASR-100B). Distributions of the so-called spreading resistance (R_s) were recorded on perpendicular inner cross-sections of the specimens. The examples depicted in Fig. 1 concern Zn diffusion of different duration at 1175 K into dislocation-free Si wafers of varying thickness. The R_s value of the p-type starting material with a resistivity around 17 $\Omega\mathrm{m}$ amounts to a few times $10^6 \, \Omega$. Obviously, Zn atoms entering from either side have reached the centre of the wafers.

Measured R_s [Ω] values were converted into resistivities ϱ [$\Omega\mathrm{m}$] with the aid of calibration data that account for the barrier resistance between probetips and the Si surface [7]. Then Zn$_s$ concentrations were calculated by the procedure described in the Appendix. Crucial in this calculation are the energy levels attributed to the double acceptor Zn$_s$. We utilized information that was recently obtained by a variety of experimental techniques on Zn-saturated specimens that the present authors had diffused: Infrared absorption spectroscopy [14] reveals for the first ionization stage $(\mathrm{Zn}_s^{0/-})$ 319 ± 3 meV above the valence band edge E_V. This value is confirmed by Hall effect measurements [12] yielding 325 ± 10 meV. Apparently the same level $(317 \pm 9$ meV) emerges from DLTS work [11, 12], which in addition determines a second ionization stage $(\mathrm{Zn}_s^{-/2-})$ 698 ± 20 meV above E_V. Both the latter energy and the much more important first level taken from the infrared study entered the present conversion of resistivity into concentration (see the Appendix).

We note that the present levels do not differ much from those reported in older work, i.e., $E_V + 0.31$ eV and
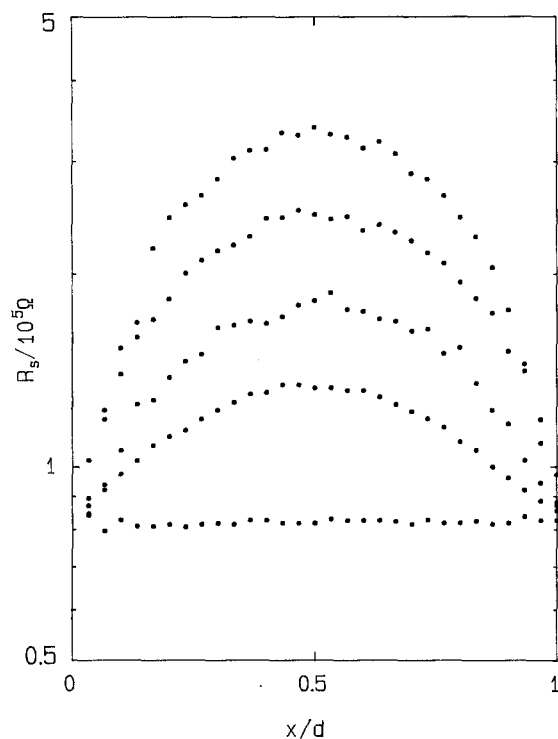
Fig. 1. Spreading-resistance profiles recorded after both-sided diffusion of Zn at 1175 K into dislocation-free Si wafers of different thicknesses d during time periods of varying length

$E_C - 0.55$ eV [15]. The previously employed energy of $E_V + 0.24$ eV detected by Hall effect analysis [5] might have originated from complex formation during the annealing treatment for the fabrication of ohmic contacts. Energies of this magnitude have been measured after low temperature annealing of pre-diffused crystals [10]. Therefore the diffusion data of Perret et al. [5] are reanalyzed in this paper on the basis of the most recent energy levels mentioned above.

Assigning diffusion-induced lowering of R_s to Zn_s would imply that Zn_i is either electrically non-active or only present in low concentration. Evidence for the latter possibility is obtained from Hall effect analysis, which reveals a compensating donor fraction of 0.003 with respect to the Zn_s solubility [12]. Also a comparison between the concentrations determined by SRT and total Zn concentrations from NAA supports the view that the overwhelming majority of Zn atoms is incorporated on substitutional sites (Sect. 2.3).

1.4 Neutron Activation Analysis

Disc-shaped, Zn-diffused specimens with a diameter of 10 mm were neutron irradiated at the nuclear research centers KFA Jülich or GKSS Geesthacht. Due to the fairly low cross-section for neutron capture (0.44 barn) irradiation times as long as 15–30 days under a thermal neutron flux 8×10^{17}–2×10^{18} m^2 s^{-2} were necessary in order to obtain enough ^{65}Zn activity through a (n, γ) reaction with the natural isotope ^{65}Zn. Simultaneously irradiated pure cobalt served for flux calibration.

After neutron activation the specimen's diameter was reduced by a multiple of the Zn penetration depth using

a special grinding machine. In this way lateral surface and lateral diffusion effects were eliminated. Depth profiling was achieved by consecutively taking off sections parallel to the circular faces with the aid of a lapping device [16]. The thickness of the sections varying between a few micrometres and several hundred micrometres was determined from the weight loss of the specimen. The 1115.6 keV γ-radiation generated by ^{65}Zn (halflife of 244.1 d) in each section was counted by means of a NaI scintillator and a multichannel analyser. Absolute concentrations were calibrated against neutron-irradiated chips of pure Zn. During the sectioning procedure the lateral homogeneity of the Zn distribution was verified by autoradiography.

2. Results and Discussion

2.1 Diffusion into Plastically Deformed Crystals

2.1.1 Experimental Data

Figure 2 shows penetration profiles measured by SRT after Zn diffusion into plastically deformed specimens. Because of the symmetrical boundary conditions only Zn_s distributions in one specimen half are displayed. The profiles are well described by the complementary error function represented by the solid lines. Table 1 compiles effective diffusion coefficients (D_{eff}) in the temperature range 1122–1473 K which result from erfc fitting. These
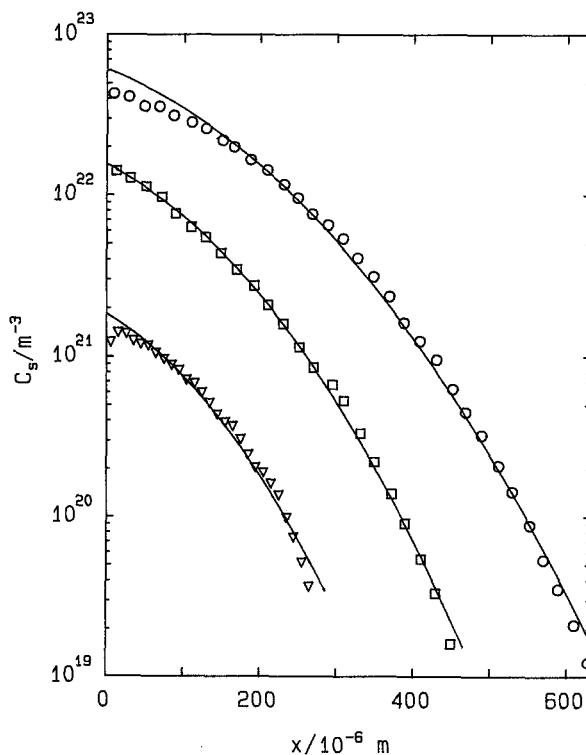

Fig. 2. Penetration profiles of Zn_s in plastically deformed Si measured by SRT. ∇ 1218 K, 7.74×10^3 s; $\square$ 1320 K, 1.8×10^3 s; o 1370 K, 1.80×10^3 s. Solid lines: erfc fit

Table 1. Diffusivity and solubility data of Zn in Si extracted from penetration profiles in plastically deformed crystals

T [K]	t [s]	D_{eff} [m^2 s^{-1}]	C_s^{eq} [m^{-3}]
1473	300	6.7×10^{-11}	1.7×10^{22}
1466	840	2.9×10^{-11}	2.4×10^{22}
1448	840	2.0×10^{-11}	1.3×10^{22}
1423	720	1.8×10^{-11}	4.0×10^{22}
1370	1800	8.3×10^{-11}	4.3×10^{22}
1320	1800	5.5×10^{-12}	1.5×10^{22}
1273	4200	3.2×10^{-12}	3.5×10^{21}
1262[a]	4320	2.8×10^{-12}	1.1×10^{22}
1218	7740	9.7×10^{-13}	1.4×10^{21}
1173	25440	3.1×10^{-13}	1.1×10^{21}
1122	73560	5.8×10^{-14}	4.0×10^{20}

[a] Reanalyzed data from [5]
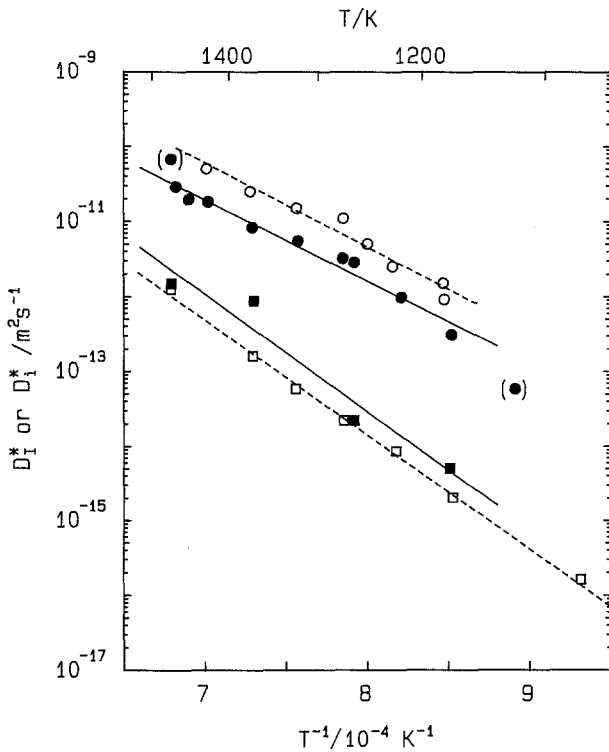
Fig. 3. Diffusion data of Zn in plastically deformed Si crystals (D_i^*, ●, upper solid line) and dislocation-free ones (D_I^*, ■, lower solid line). Comparable data of Au (○, □, dashed lines) are also shown

data closely follow the Arrhenius relationship

$$D_{\text{eff}} = \left(6.9 \begin{array}{c} +14 \\ -4.6 \end{array} \right)$$
$$\times 10^{-4} \exp(-2.14 \pm 0.12\, eV\, /kT)\, \text{m}^2\, \text{s}^{-1}, \qquad (3)$$

as revealed by the filled circles and the upper solid line in Fig. 3. In (3), k denotes Boltzmann's constant and T absolute temperature.

Profiles of erfc shape point to a constant diffusivity nourished from an inexhausted Zn source maintaining a fixed concentration at $x = 0$. This boundary concentration may therefore be considered as the solubility at the temperature and the particular Zn pressure – in equilibrium with

pure Zn – during diffusion annealing. Accordingly, the boundary concentrations determined by SRT are listed in Table 1 under C_s^{eq}.

2.1.2 Interpretation

The present diffusivities are extremely large when one realizes that they pertain to a substitutional species, i.e. Zn$_s$. Such large values cannot be explained by lattice-site-to-lattice-site exchanges via vacancies (see discussion in [17]). This compels us to consider diffusion involving interstitial-substitutional exchange. Within the framework of both the kick-out and the dissociative mechanism the diffusivity in highly dislocated crystals is given by [4–7]

$$D_{\text{eff}} = D_i^* \equiv \frac{C_i^{\text{eq}} D_i}{C_i^{\text{eq}} + C_s^{\text{eq}}} \approx \frac{C_i^{\text{eq}} D_i}{C_s^{\text{eq}}} \qquad (4)$$

accounting for $C_s^{\text{eq}} \gg C_i^{\text{eq}}$. This expression reflects that the Zn$_s$ incorporation rate is not determined by the properties of I or V but only by the fraction of the mobile Zn$_i$ species $C_i^{\text{eq}}/C_s^{\text{eq}}$ and its diffusivity D_i. The reason is that dislocations form efficient sinks or sources for self-interstitials and vacancies. Deviations from intrinsic point-defect equilibrium induced by the kick-out or dissociative reactions (1, 2) are quasi-immediately levelled off through generation and annihilation processes associated with dislocation climb.

Interpreting D_{eff} according to (4) further implies that Zn segregation at dislocations only plays a minor role. In principle this phenomenon would reduce the mobile atom fraction to $\bar{C}_i^{\text{eq}}/(C_s^{\text{eq}} + \bar{C}_d^{\text{eq}})$ where $\bar{C}_d^{\text{eq}}$ denotes the average volume density of (heterogeneously) segregated Zn in equilibrium with C_s^{eq}. However, TEM examination of our specimens did not reveal clear indications of Zn segregation.
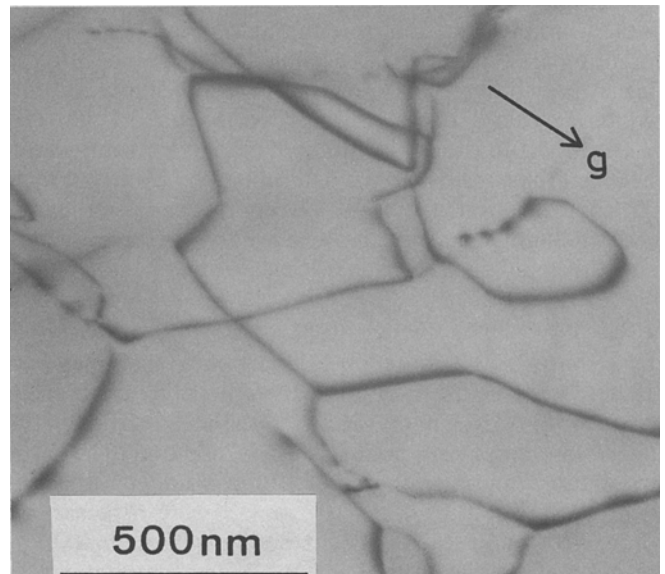

Fig. 4. Cross-sectional TEM micrograph showing dislocations in the Zn-diffused region of the plastically deformed specimen containing the lowest profile in Fig. 2

Figure 4 shows a TEM micrograph of the specimen containing the lowest profile in Fig. 2. This cross-sectional observation was made in a JEOL 2000EX operated at 200 kV. It reveals the dislocation structure within the diffusion zone near the surface, but no salient features with regard to segregation or precipitation are seen. Similar images originate from other regions of the specimen.

Figure 3 exhibits diffusion coefficients of Au in plastically deformed Si by open circles. The associated upper dashed line is characterized by an activation energy of 2.23 eV and a pre-exponential factor of $44 \times 10^{-4}\,\mathrm{m^2\,s^{-1}}$. These parameters result from Arrhenius fitting of the original data given in [7]. As is seen in Fig. 3, Zn and Au behave rather similarly. This supports the present interpretation since Au has been shown to migrate via interstitial-substitutional exchange [7,18].

2.2 Diffusion into Dislocation-Free Crystals

2.2.1 Spreading-Resistance Data

U-shaped profiles. Figure 5 shows concentration-depth profiles that were calculated from the SRT measurements in Fig. 1 by the procedure described in the Appendix. In these cases the entire width of the dislocation-free Si slices is displayed. The family of U-shaped curves in Fig. 5 reflects the gradual diffusion-controlled accumulation of Zn_s in Si at 1175 K up to complete saturation. Comparing the profile shape in the left half of the slices
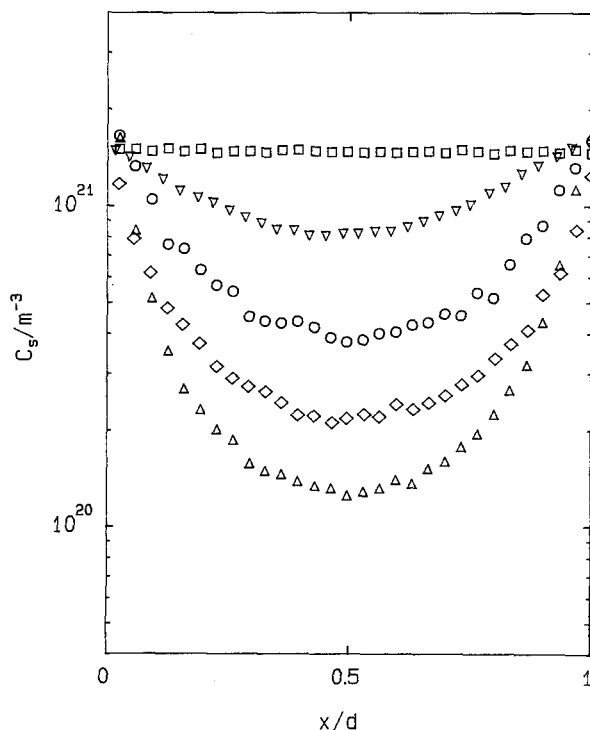
Fig. 5. Penetration profiles on Zn_s in dislocation-free Si wafers deduced from the SRT measurements in Fig. 3. △ wafer thickness $d = 1200\,\mu m$, annealing time $t = 1.77 \times 10^5\,s$; ◇ 1200 μm, 4.37×10^5 s; ○ 1200 μm, 1.10×10^6 s; ▽ 300 μm, 3.45×10^5 s; □ 286 μm, 1.47×10^6 s
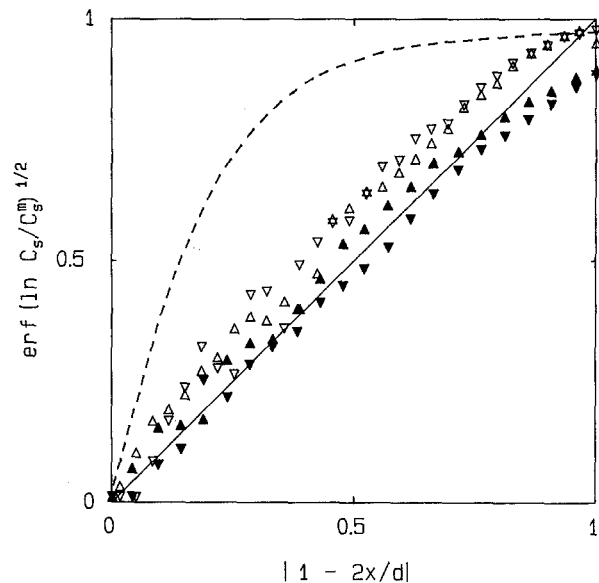
Fig. 6. Comparison of U-shaped Zn_s profiles in dislocation-free Si with the theoretical prediction of the kick-out model (solid line). △ 1175 K, 1200 μm, 1.77×10^5 s, $x < d/2$; ▽ the same, but $x > d/2$; ▲ 1370 K, 2200 μm, 1.93×10^4 s, $x < d/2$; ▼ the same, but $x > d/2$. Dashed line: erfc-like penetration from opposite sides

after short annealing times with corresponding plots of $\log C_s$ vs. x in plastically deformed Si (Fig. 2), one notices the pronounced difference in curvature. The non-erfc profiles of Fig. 5 are reminiscent of Au distributions in dislocation-free Si and hence indicative of kick-out diffusion [18].

Analysis of profile shape. Figure 6 enables a closer examination of the profile shape. In this special plot the kick-out model is represented by the straight line with slope 1 given by [6]

$$\mathrm{erf}\left(\ln\frac{C_s}{C_s^m}\right)^{1/2} = \left|1 - \frac{2x}{d}\right|. \qquad (5)$$

Here, C_s^m denotes the concentration in the middle of the Si slice having a thickness d. Equation (5) forms a good approximation as long as (i) $C_s \lesssim 0.5 C_s^{eq}$ and provided that (ii) Zn_i has attained its solubility limit throughout the specimen.

It is seen in Fig. 6 that the kick-out prediction almost matches an originally U-shaped profile measured at 1370 K (black triangles). The deviation at the right hand side is connected with the violation of the above condition (i). The lowest profile of Fig. 5 (open triangles) also follows the straight line in Fig. 6 but somewhat shifted upwards. This may be due to the circumstance that the above requirement (ii) is not fulfilled for this comparatively short annealing time (1.77×10^5 s, $d = 1.2\,mm$, $T = 1175\,K$). The upward shift may also be related to electrical activity of Zn_i, the low but probably non-negligible Zn_s concentration C_s^0 [6] which is established in mass-action-law equilibrium with C_i^{eq} shortly after the beginning of the diffusion anneal, or to fast diffusing unwanted impurities.

The observed shift with respect to the (idealized) kick-out prediction [straightline, (5)] indicates a change of profile towards more erfc character. This becomes clear from comparison with the dashed line in Fig. 6, which represents erfc-like penetration from opposite surfaces overlapping in the middle [18]. This hypothetical profile was adjusted to the lower profile in Fig. 5 (open triangles in Fig. 6) by taking the concentrations at the boundary and in the middle as fixed points. Obviously, the experimental data are closer to the kick-out prediction.

Evaluation of Diffusion Rate. Having examined the profile shapes, an effective diffusion coefficient can be extracted from the increase of the middle concentration C_s^m as a function of annealing time. Kick-out theory predicts for dislocation-free Si [4–7]

$$\frac{C_s^m}{C_s^{eq}} = \frac{2}{d}\left(\pi D_I^* t\right)^{1/2},\tag{6}$$

where

$$D_I^* = \frac{C_I^{eq} D_I}{C_s^{eq}}\tag{7}$$

contains the equilibrium concentration of self-interstitials C_I^{eq}, their diffusivity D_I and the Zn_s solubility C_s^{eq}. This behaviour is illustrated in Fig. 7 for measurements at 1175 K (Fig. 5). By fitting (6) (solid line) to the data we find $D_I^* = 5.0 \times 10^{-15}\,\mathrm{m^2\,s^{-1}}$. This value and similar data at other temperatures are collected in Table 2.

The dashed line in Fig. 7 reproduces the erfc-like increase of C_s^m expected if the Zn_s incorporation were governed by the dissociative mechanism, see (2) [18]. The diffusivity holding in that case, i.e. $D_V^* = C_V^{eq} D_V / C_s^{eq}$ (in self-explanatory notation) was calculated by using existing $C_V^{eq} D_V$ data [19]. Obviously, the dissociative model

Table 2. Diffusivity and solubility data of Zn in Si deduced from families of U-shaped penetration profiles in dislocation-free wafers

T [K]	C_s^{eq} [m^{-3}]	D_I^* [m^2 s^{-1}]	$C_s^{eq} D_I^*$ [a] [m^2 s^{-1}]
1473	5.2×10^{22}	1.5×10^{-12}	1.6×10^{-18}
1370	1.5×10^{22}	8.7×10^{-13}	2.6×10^{-19}
1262	1.3×10^{22}	2.2×10^{-14}	5.7×10^{-21}
1175	1.5×10^{21}	5.0×10^{-15}	1.5×10^{-22}

[a] In this product C_s^{eq} enters as a fraction of the Si lattice site density $C_0 = 5.0 \times 10^{28}\,\mathrm{m^2\,s^{-1}}$

cannot account for the observed qualitative and quantitative behaviour.[1]

The predominance of the kick-out mechanism was established by similar measurements in the range 1175 K–1473 K (Table 2). In all cases the solubility C_s^{eq} was determined on specimens diffused to saturation. Resulting D_I^* values are plotted in Fig. 3 as closed squares together with similar data from Au diffusion experiments (open squares). The best-fitted Arrhenius relationship to the Zn data (lower solid line) reads

$$D_I^* = 0.10\exp(-3.11\,eV\,/kT)\,\mathrm{m^2\,s^{-1}},\tag{8}$$

whereas the corresponding expression for Au in dislocation-free Si (lower dashed line) is characterized by an activation energy of 3.03 eV and a pre-exponential factor of 0.023 m^2 s^{-1}.

The close similarity between the D_I^* values of these elements implies according to (7) that their C_s^{eq} data are not far apart. This is confirmed by comparing the Zn solubilities in Sect. 2.3 (Fig. 11) with those of Au reported in [20].[2]

Interrelationship Between the Zn Incorporation Rate and Si Self-Diffusion. According to (7), D_I^* contains $C_I^{eq} D_I$. This is the contribution of self-interstitials to the (uncorrelated) Si self-diffusivity provided that C_I^{eq} is given as an atomic fraction (Si lattice site density $C_0 = 5.0 \times 10^{28}\,\mathrm{m^3}$). Hence this contribution can be extracted from the diffusion and solubility data on dislocation-free Si using

$$C_I^{eq} D_I = C_s^{eq} D_I^*\tag{9}$$

with C_s^{eq} given as an atomic fraction as well. Quantitative results obtained by SRT are listed in Table 2.

For comparison with the self-diffusion coefficient D^T measured by Si tracers we must account for diffusion correlation effects. In agreement with similar work on Au or Pt in Si [18, 20, 21] the self-interstitial-related correlation factor is taken as 1/2 (which equals the correlation fac-
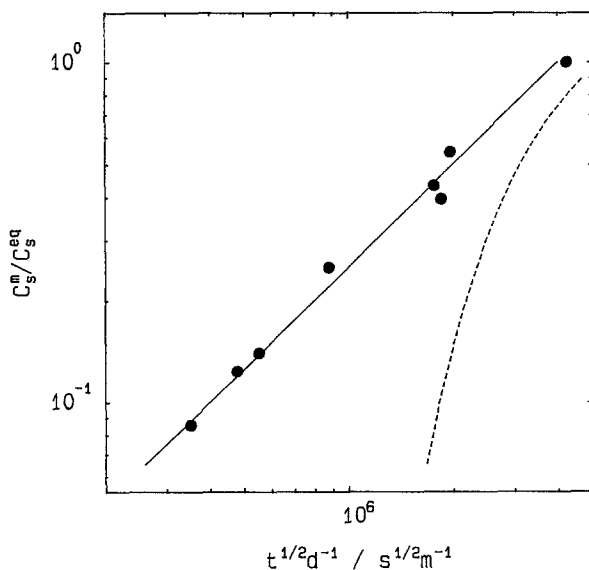

Fig. 7. Double logarithmic plot to check how the relative Zn_s concentration in the middle of dislocation-free Si wafer depends on annealing time t and wafer thickness d. Solid line: kick-out mechanism; dashed line: dissociative mechanism

[1] Equation (6) is a good approximation as long as C_s^m does not come too close to C_s^{eq}. Surprisingly, the $\sqrt{t}$ increase in Fig. 7 appears to be fulfilled for $0.5 \leq C_s^m/C_s^{eq} < 1$ as well. This may be explained by a minor but noticeable contribution of the dissociative mechanism to the diffusion process. As revealed by Fig. 7, the dissociative component (dashed line) increases with respect to the kick-out component (solid line) as the concentration rises

[2] Strictly, the finding that D_I^* is described by an Arrhenius equation can only be approximately true because of the retrograde nature of the Zn or Au solubility (Fig. 11). Furthermore, the scatter of $D_I^*(Zn)$ around (8) seen in Fig. 3 may be due to C_s^{eq} variations caused either by differences in the partial Zn pressure or by less accurate determination of the solubility limit by means of SRT
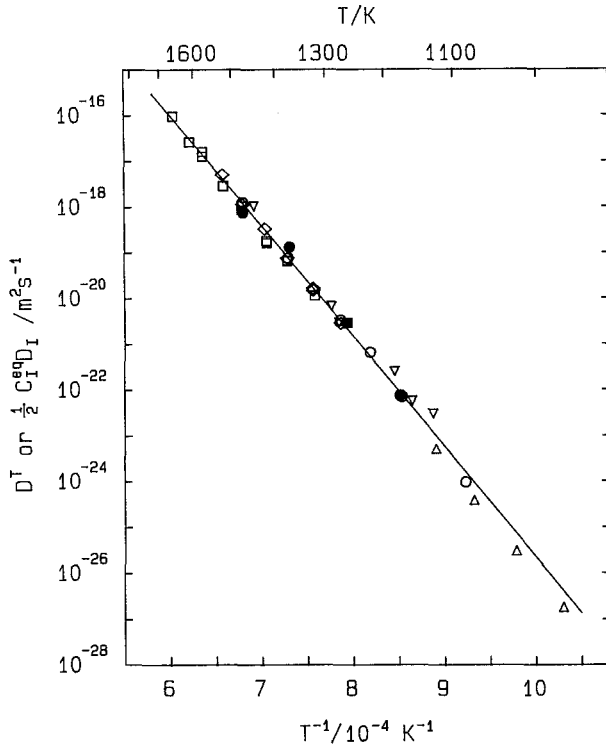
Fig. 8. Self-diffusion coefficients of Si, including D^T values directly measured by means of Si tracers ($\square$ [24]), ∇ [25]) and $\frac{1}{2} C_I^{eq} D_I$ data deduced from the diffusivity and solubility of Au ($\circ$ [18, 20]), Pt ($\diamond$ [21], $\triangle$ [23]) and Zn ($\bullet$, $\blacksquare$: this work, [5]). The solid line was fitted to $\bullet$, $\blacksquare$, $\circ$ and $\diamond$

Fig. 9. Depth distribution of the total Zn concentration determined by NAA on a 5 mm-thick, dislocation-free Si specimen after a diffusion anneal of 3300 s at 1474 K. Solid line: theoretical kick-out profile; dotted line: erfc profile

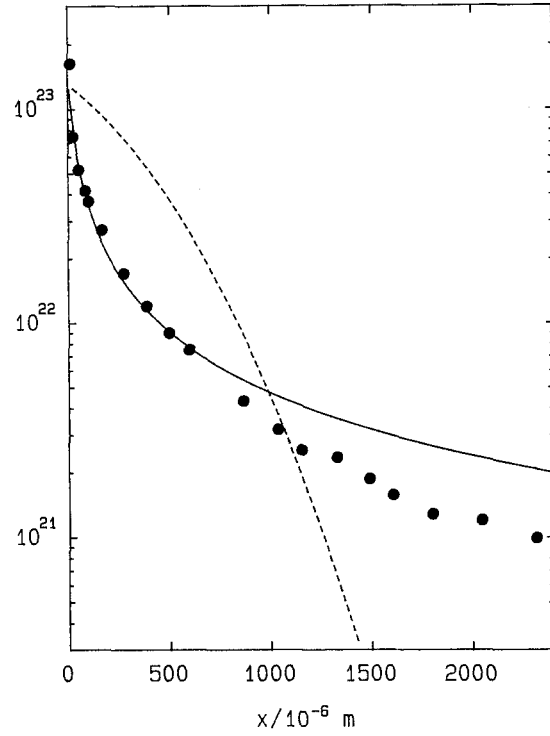tor for the vacancy mechanism in the diamond structure [22]).

Figure 8 shows that the $\frac{1}{2} C_I^{eq} D_I$ data of the present Zn study agree with similar values from Au and Pt experiments. Least-squares fitting to these three sets of data yields

$$C_I^{eq} D_I = \left(600 \begin{array}{c} +460 \\ -260 \end{array} \right)$$

$$\times 10^{-4} \exp(-4.79 \pm 0.06 \, eV \, /kT) \, \mathrm{m^2 \, s^{-1}}. \qquad (10)$$

Multiplied by 1/2, this equation is represented in Fig. 8 by the solid line, which also runs close to the low temperature, Pt-related data from the DLTS work of Mantovani et al. [23]. Further, it is seen that directly measured tracer self-diffusivities [24, 25] are fairly well covered by (10). This provides evidence that, in Si, self-interstitials contribute substantially to D^T. However, the vacancy component of the self-diffusion coefficient cannot be totally neglected, especially at low temperatures. For a discussion of this topic we refer to [19, 26].

2.2.2 Neutron Activation Data

A few concentration-depth profiles were measured after neuron irradiation of effectively thin, Zn-diffused wafers. Here the overlap of the diffusion fronts entering from opposite surfaces was sufficient to produce distributions well described by (5). Also values of D_I^* deduced by the

use of (6) and $C_I^{eq} D_I$ through (9) are consistent with (8) and (10), respectively.

Figure 9 reveals the variation of the total Zn concentration $C_t (= C_s + C_i + \dots)$ in one half of a 5 mm-thick, dislocation-free specimen. The data result from serial sectioning in conjunction with NAA after 3300 s of annealing at 1474 K. Clearly, the experimental profile deviates from the complementary error function (dotted line) that reflects both qualitatively and quantitatively the diffusion behaviour in plastically deformed Si (Sect. 2.1). In contrast, the near-surface data are well described by

$$\frac{C_s}{C_s^{eq}} = \left[1 - a_0 \left(\frac{x}{D_I^* t} \right)^{1/2} \right]^{-1} \qquad (11)$$

approximating the theoretical kick-out profile [27, 28]. The dimensionless parameter a_0 usually takes values between -1 and -3 [19, 28]. Choosing $a_0 = -2$ one obtains from fitting of (11) D_I^* (1474 K) $= 1.6 \times 10^{-12} \, \mathrm{m^2 \, s^{-1}}$ in accordance with Table 2. Further, multiplication by the (fitted) boundary concentration of $1.3 \times 10^{23} \, \mathrm{m^{-3}} / C_0 (= 2.6 \times 10^{-6})$ yields on the basis of (9) $C_I^{eq} D_I = 4.2 \times 10^{-18} \, \mathrm{m^2 \, s^{-1}}$, which is close to (10).

The above analysis confirms that the kick-out-like features discussed in previous sections are not artefacts of the spreading-resistance measurement but real. Moreover, the circumstance that NAA measures the total concentration whereas (11) holds for C_s alone discloses once more the predominance of Zn_s in the high concentration

region. On the other hand, the deviation of the theoretical profile from the data at lower concentrations relates to the violation of $C_i = C_i^{eq}$ assumed in the derivation of (11). Since D_i is finite, the supply of Zn_i atoms from the surface breaks down beyond some penetration distance provided that the specimen is thick enough to reveal this feature. A theoretical estimation of the critical concentration $C_s^* (\cong C_t^*)$ below which this phenomenon becomes manifest is given by $C_s^*/C_s^{eq} = D_I^*/D_i^*$ [29]. For 1474 K we obtain with the aid of (3) and (8) $C_s^* = 5 \times 10^{21} \, \text{m}^{-3}$. This agrees with the graphical information from Fig. 9.

2.3 Solubility

2.3.1 Neutron Activation Data

Successful solubility measurements with NAA were carried out between 1275 K and 1484 K. The homogeneity of the ^{65}Zn distribution after sufficiently long annealing was verified by means of sectioning and radioactive counting as illustrated in Fig. 10. In two cases where saturation in the centre part of the 0.5 mm-thick wafers was not fully achieved, the solubility was taken from the near-boundary concentration (upper data in Fig. 10). The about 30% deviation of the mid concentration from the solubility limit was found to be consistent with (6) for the given duration of annealing. The experimental error in the solubility measurement is estimated to be about 30%, which mainly arises from uncertainties in the neutron flux.

Solubility data from NAA are listed in Table 3 and plotted in Fig. 11 as filled circles. A too low saturation value of $7.0 \times 10^{21} \, \text{m}^{-3}$ determined at 1557 K (lowest data in Fig. 10) is omitted, since at this high temperature the Zn diffusion source was reduced in order to prevent the quartz ampoule from swelling and cracking.

Based on the SiZn phase diagram a (thin) liquid layer will form on the surface of the specimens when after prolonged annealing enough Zn has been transferred via the vapour phase. This seemed to be the case in our solubility (and diffusion) experiments, as indicated by the appearance of the samples after the annealing treatment. Even after removal of the Zn-rich surface layer by etching, the first sections of the depth-profile measurements contained Zn concentrations up to $10^{26} \, \text{m}^{-3}$. Such high near-surface data have been discarded in Fig. 10.

The composition of the surface liquid may deviate from the liquidus curve in the ambient pressure equilib-
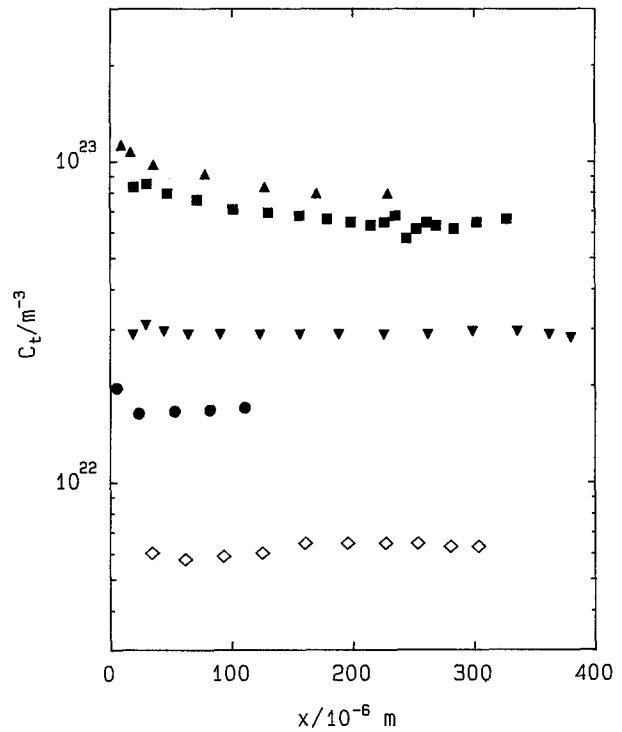

Fig. 10. Zn distributions in (almost) saturated, dislocation-free Si wafers of 0.5 mm thickness as measured by NAA. ▲ 1484 K, ■ 1475 K, ▼ 1379 K, ● 1327 K, ◇ 1557 K (too low Zn pressure)
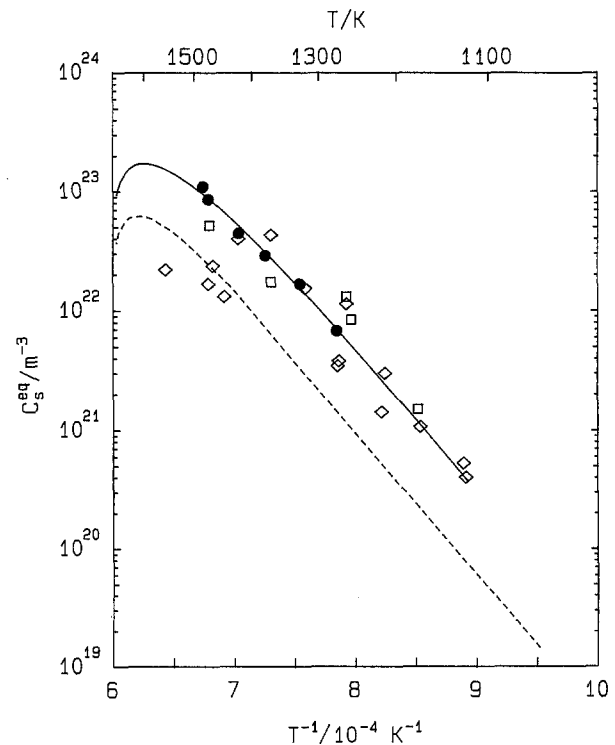

Fig. 11. Solubility data of Zn in crystalline Si, including saturation concentrations in dislocation-free Si by NAA (●) or SRT (□) and boundary concentrations in plastically deformed Si by SRT (◇). Solid curve: fit based on "ideal" solution model; dashed curve: data of [30–32]

Table 3. Solubility data of Zn in Si determined by NAA on (almost) saturated specimens 0,5 mm thick (exception 1422 K : 1.0 mm)

T [K]	t [s]	C_s^{eq} [m^{-3}]
1275	5.15×10^5	6.4×10^{21}
1327	4.11×10^5	1.7×10^{22}
1379	2.47×10^5	2.9×10^{22}
1422	4.97×10^5	4.5×10^{22}
1475	7.20×10^3	8.6×10^{22}
1484	7.92×10^3	1.1×10^{23}

rium phase diagram because of the relatively high vapour pressure imposed by pure Zn. Consequently, the present solid solubilities may exceed slightly those values that would establish after exhaustion of the elemental diffusion source. Nevertheless, the present data form a definite set by virtue of the unambiguous boundary conditions which were similar in all experiments. From the presence of pure Zn in the quartz ampoule after saturation annealing we conclude that the Zn source was sufficiently large to maintain its partial pressure.

The solid curve in Fig. 11 represents the fitted "ideal" solubility of Zn in crystalline Si assuming that also the SiZn liquid may be described by the ideal-solution model [1]. This predicts a maximum solubility of $2.5 \times 10^{23}\,\mathrm{m^{-3}}$ at 1598 K, as seen in Fig. 11. We further obtain from the best fit an enthalpy of 2.49 eV and an entropy of $7.26\,k$, both of which are associated with transferring one Zn atom from the liquid to the solid phase. Accordingly, the segregation coefficient at the melting point results as 5.05×10^{-5}.

2.3.2 Spreading-Resistance and Literature Data

In addition to the NAA results, Fig. 11 exhibits solubility data from SRT as open symbols. Both saturation values in dislocation-free specimens (squares, see Sect. 2.2.1) and boundary concentrations in plastically deformed crystals (diamonds, see Sect. 2.1.1) are included. These electrical data agree fairly well with the chemical ones, disregarding several low SRT values at high temperatures. Such low solubilities may be due to exhaustion of the diffusion source by progressive alloying of Zn with Si.[3]

The dashed line in Fig. 11 originating from data of Blouke et al [30] also covers the older data of Carlson [31] and Fuller and Morin [32]. The departure towards smaller concentrations with respect to the present data is quite understandable, since the original authors report partial pressures which, particularly at the high temperature side, are below the equilibrium values referring to pure Zn at the diffusion temperature. At the low temperature side saturation may not always have been attained in the older experiments, as can be estimated from the present diffusion data.

3. Summary

1) Zn diffusion in Si mainly takes place through the kick-out mechanism. Here interstitial(Zn_i)-substitutional(Zn_s) exchange is mediated by self-interstitials (I) as reflected by (1).

2) Zn_s dominates over (Zn_i) and hence determines the solubility.

3) The effective diffusivity of Zn in plastically deformed Si is quantitatively described by (3). Its interpretation according to (4) in terms of Zn_i-controlled penetration of Zn_s relies on the presence of dislocations, which provide a high density of sinks for self-interstitials.

4) Segregation of Zn at dislocations does not play a significant role.

5) Incorporation of Zn in dislocation-free crystals is governed by the flow of self-interstitials to the surface as expressed by (7). The temperature-dependent incorporation-rate is approximated by (8).

6) The diffusion behaviour of Zn in Si is very similar to that of Au, as illustrated by Fig. 3.

7) The self-interstitial component $C_I^{eq}D_I$ of the (uncorrelated) Si self-diffusion coefficient can be calculated on the basis of (9) from Zn diffusion and solubility data in dislocation-free Si. Equation (10) provides the resulting Arrhenius expression, which also includes similar data from Au and Pt experiments.

Appendix

The procedure for the conversion of resistivities ϱ into Zn_s concentrations C_s is outlined below. Starting from the charge neutrality condition we have

$$n + C_A^- + C_{Zn}^- + 2C_{Zn}^{2-} = p + C_D^+, \tag{A1}$$

where, in addition to electrons (n), holes (p) and the two ionization stages of the (Zn_s) double acceptor (C_{Zn}^-, C_{Zn}^{2-}), allowance is made for shallow acceptors (C_A^-) and/or shallow donors (C_D^+). Analogous to the well-known ionization ratios of group III and group V dopants [33], i.e.

$$C_A^-/C_A^0 = g_A \exp[-(E_A - E_F)/kT] \tag{A2}$$

with $g_A = 1/4$ and

$$C_D^+/C_D^0 = g_D^{-1} \exp[-(E_D - E_F)/kT] \tag{A3}$$

with $g_D = 2$, we define for $j = 1, 2$ [34]

$$w_j \equiv C_{Zn}^{j-}/C_{Zn}^{(j-1)-} = g_j \exp[-(E_j - E_F)/kT]. \tag{A4}$$

Here E_F is the Fermi level while $E_1 = 319\,\mathrm{meV}$ and $E_2 = 698\,\mathrm{meV}$ are the Zn_s acceptor levels with respect to the valence band edge $E_V \equiv 0$. The degeneracy factors $g_1 = 1$ and $g_2 = 1/4$ reflect the existence of two valence bands as well as the electronic configuration of the Zn atom. The total Zn_s concentration is given by the sum of neutral and ionized atoms, i.e.

$$C_s = C_{Zn}^0 + C_{Zn}^- + C_{Zn}^{2-}. \tag{A5}$$

---

[3] The remaining scatter around the solid curve can be largely explained by wear effects on the two point probes used by SRT. More frequent calibration would have been necessary to account for this phenomenon. Also, a higher density of calibration data in an appropriate resistivity regime would have enhanced the overall accuracy

Inserting (A4) into (A1) and (A5) yields after elimination of C_{Zn}^0

$$C_s = \frac{1 + w_1 + w_1 w_2}{w_1 + 2w_1 w_2} (p - n + C_D^+ - C_A^-). \tag{A6}$$

Under non-degenerate conditions holding for our Zn-diffused crystals at room temperature the hole density p is calculated from ϱ through

$$p = \frac{1}{2\varrho q \mu_p} + \sqrt{\frac{1}{(2\varrho q \mu_p)^2} - n_i^2 \frac{\mu_n}{\mu_p}} \tag{A7}$$

with elementary charge q, mobility of holes μ_p and electrons μ_n and the intrinsic electron density n_i. Then n and E_F are obtained from

$$np = n_i^2 = N_C N_V \exp(-E_g/kT) \tag{A8}$$

and

$$E_F = E_V - kT \ln(p/N_V). \tag{A9}$$

Knowing the effective density of states (at 296 K) in the valence band ($N_V = 2.66 \times 10^{25} \mathrm{m}^{-3}$; from a relative effective hole mass of 1.04 [35]) and conduction band ($N_C = 3.22 \times 10^{25} \mathrm{m}^{-3}$; from a relative effective electron mass of 1.18 [36]), the intrinsic mobilities ($\mu_p^{max} = 0.0495 \, \mathrm{m^2 \, V^{-1} \, s^{-1}}$, $\mu_n^{max} = 0.136 \, \mathrm{m^2 \, V^{-1} \, s^{-1}}$ [37]) and the energy gap ($E_g = 1.125 \, \mathrm{eV}$ [38]), we substitute (A4, A7–A9) into (A6) to yield C_s.

Scattering of the majority charge carriers by ionized atoms is taken into account by the empirical relationship [33]

$$\mu_p = \mu_p^{min} + \frac{\mu_p^{max} - \mu_p^{min}}{1 + (C^{ion}/C_p^{ref})^{\alpha_p}} \tag{A10}$$

with $\mu_p^{min} = 4.77 \times 10^{-3} \, \mathrm{m^2 \, V^{-1} \, s^{-1}}$, $C_p^{ref} = 6.3 \times 10^{22} \, \mathrm{m}^{-3}$ and $\alpha_p = 0.76$. Here C^{ion} denotes the effective concentration of charged atoms ($C_{Zn}^- + 2C_{Zn}^{2-} + C_A^- + C_D^+$). Iterating p, n, E_F and C_s by the use of (A1) with $C^{ion} = 0$ as the initial value leads to rapid convergence.

References

1. E.R. Weber: Appl. Phys. A **33**, 1 (1983)
2. D. Gilles, W. Bergholz, W. Schröter: J. Appl. Phys. **59**, 3590 (1986)
3. J. Utzig, D. Gilles: Mater. Sci. Forum **38–41**, 729 (1989)
4. W. Frank, U. Gösele, H. Mehrer, A. Seeger: In *Diffusion in Crystalline Solids*, ed. by G.E. Murch, A.S. Nowick (Academic, New York 1984) p. 64
5. M. Perret, N.A. Stolwijk, L. Cohausz: J. Phys.: Condes. Matter **1**, 6347 (1989)
6. U. Gösele, W. Frank, A. Seeger: Appl. Phys. **23**, 361 (1980)
7. N.A. Stolwijk. J. Hölzl, W. Frank, E.R. Weber, H. Mehrer: Appl. Phys. A **39**, 37 (1986)
8. F.C. Frank, D. Turnbull: Phys. Rev. **104**, 617 (1956)
9. I. Yonenaga, U. Onose, K. Sumino: J. Mater. Res. **2**, 252 (1987)
10. S. Weiss, R. Beckmann, R. Kassing: Appl. Phys. A **50**, 151 (1990)
11. P. Stolz, G. Pensl, D. Grünebaum, N.A. Stolwijk: Mater. Sci. Eng. B **4**, 31 (1989)
12. P. Stolz: Thesis, University of Erlangen-Nürnberg (1990)
13. H.E. Altink, T. Gregorkiewicz, C.A.J. Ammerlaan: Solid State Commun. **75**, 115 (1990)
14. A. Dörnen, R. Kienle, K. Thonke, P. Stolz, G. Pensl, D. Grünebaum, N.A. Stolwijk: Phys. Rev. B **40**, 12005 (1989); Mater. Res. Soc. Symp. Proc. **163**, 21 (1990)
15. J.W. Chen, A.G. Milnes: Annu. Rev. Mater. Sci. **10**, 157 (1980)
16. L.M.L.J. Leblans, M.L. Verheijke: Philips Tech. Rev. **25**, 191 (1963/1964)
17. A. Almazouzi, H. Bracht, J. Bernardini, E.G. Moya, N.A. Stolwijk, H. Mehrer: J. Appl. Phys. (in press)
18. N.A. Stolwijk, B. Schuster, J. Hölzl: Appl. Phys. A **33**, 133 (1984)
19. T.Y. Tan, U. Gösele: Appl. Phys. A **37**, 1 (1985)
20. N.A. Stolwijk, B. Schuster, J. Hölzl, H. Mehrer, W. Frank: Physica **116B**, 335 (1983)
21. J. Hauber, W. Frank, N.A. Stolwijk: Mater. Sci. Forum **38–41**, 707 (1989)
22. A.D. Le Claire: Phys. Chem. **10**, 261 (1970)
23. S. Mantovani, F. Nava, C. Nobili, G. Ottaviani: Phys. Rev. B **33**, 5336 (1985)
24. H.J. Mayer, H. Mehrer, K. Maier: Inst. Phys. Conf. Ser. **31**, 186 (1977)
25. L. Kalinowski, R. Seguin: Appl. Phys. Lett **42**, 680 (1983)
26. F. Morehead, N.A. Stolwijk, W. Meyberg, U. Gösele: Appl. Phys. Lett **42**, 690 (1983)
27. A. Seeger: Phys. Status Solidi A **61**, 521 (1980)
28. U. Gösele, F. Morehead, W. Frank, A. Seeger: Appl. Phys. Lett **38**, 157 (1981)
29. N.A. Stolwijk: Unpublished
30. M.M. Blouke, N. Holonyak, Jr., B.G. Streetman, H.R. Zwicker: J. Phys. Chem. Solids **31**, 173 (1970)
31. R.O. Carlson: Phys. Rev. **108**, 1390 (1957)
32. C.S. Fuller, F.J. Morin: Phys. Rev. **105**, 379 (1957)
33. S.M. Sze: *Physics of Semiconductor Devices*, 2nd edn. (Wiley, New York 1981)
34. W. Shockley, J.T. Last: Phys. Rev. **107**, 392 (1957)
35. R.G. Humphreys: J. Phys. C **14**, 2935 (1981)
36. H.D. Barber: Solid-State Electron. **10**, 1039 (1967)
37. C. Jacobini, C. Canali, G. Ottaviani, A. Alberigi Quaranta: Solid-State Electron. **20**, 77 (1977)
38. C.D. Thurmond: J. Electrochem. Soc. **122**, 1133 (1975)